Earth Planet. Sci. Lett. 625 (2024) 118499

Contents lists available at ScienceDirect

Earth and Planetary Science Letters

journal homepage: www.elsevier.com/locate/epsl

Iron isotope evidence in continental intraplate basalts for mantle lithosphere imprint on heterogenous asthenospheric melts

Rong Xu [a,*], Sarah Lambart [b], Oliver Nebel [c], Ming Li [d,*], Zhongjie Bai [a], Junbo Zhang [d], Ganglan Zhang [e], Jianfeng Gao [a], Hong Zhong [a], Yongsheng Liu [d]

[a] State Key Laboratory of Ore Deposit Geochemistry, Institute of Geochemistry, Chinese Academy of Sciences, Guiyang 550081, China
[b] Geology and Geophysics, University of Utah, Salt Lake City, UT, United States
[c] School of Earth, Atmosphere and Environment, Monash University, 3800 Clayton, VIC, Australia
[d] State Key Laboratory of Geological Processes and Mineral Resources, School of Earth Sciences, China University of Geosciences, Wuhan 430074, China
[e] Key Laboratory of Marine Mineral Resources of Ministry of Natural Resources, Guangzhou Marine Geological Survey, Guangzhou 511458, China

ARTICLE INFO

Editor: Dr R. Hickey-Vargas

Keywords:
Alkali basalt
Fe isotopes
Pyroxenite
Asthenosphere
Lithosphere

ABSTRACT

Iron isotope studies on ocean island basalts (OIBs) and mid-ocean ridge basalts (MORBs) have disclosed the contribution of pyroxenite lithologies in the generation of basaltic magmas. Whether Fe isotopic compositions of continental intraplate basalts can be applied to trace lithological heterogeneity within the mantle source regions remains poorly investigated. To explore the systematics of stable Fe isotopes as a potential probe of lithological heterogeneity in the source of continental intraplate basalts, we present twenty-four Fe isotope data on a suite of well-characterized Cenozoic basalts from SE China. The samples show a large range of Fe isotope values (δ^{56}Fe = +0.09‰ to +0.20‰), which correlate with SiO_2, CaO/Al_2O_3, Ti/Eu, Hf/Hf*, Zr/Nb, Dy/Yb, La/Yb, Nb/Y, K/La, Sr/Ce, δ^{66}Zn and estimated equilibrium pressures. The samples with the highest δ^{56}Fe values represent early-stage low-silica basalts with moderately enriched Sr-Nd isotope ratios and high δ^{66}Zn values, while the late-stage high-silica basalts display a broad δ^{56}Fe decrease with increasing $^{87}Sr/^{86}Sr$ and with decreasing ε_{Nd} and δ^{66}Zn. We demonstrate that the heaviest Fe isotope signatures cannot be derived from a pure peridotite source and require a pyroxenite component in the source. Combined with other geochemical proxies, we show that the heaviest basalt compositions are consistent with low-degree melts produced by the adiabatic decompression of a carbonated pyroxenite-bearing asthenospheric mantle. Mixing of these hybrid melts with melt produced from in-situ melting of the subduction-modified sub-continental lithospheric mantle (SCLM) reproduces the Fe-isotope variability of the late-stage basalts. Our results demonstrate the significance of lithological heterogeneity in the mantle source of continental intraplate basalts and highlight the subsequent imprint of mantle lithosphere in the evolution of their Fe isotope compositions. Finally, this study exemplifies the potential of the Fe-Zn stable isotope pair for mantle geochemistry; coupled with traditional radiogenic isotopes and major and trace element concentrations, they formed an efficient tool to trace the nature and contribution of the mantle source components in the formation of intraplate basalts.

1. Introduction

The formation of ocean island basalts (OIBs) is generally attributed to shallow emplacement of hot upwelling heterogeneous mantle plumes (Hofmann, 1997; White, 2010). The wide diversity in major and trace element and radiogenic isotope compositions of OIBs corroborates that their mantle source regions are highly heterogeneous. Subducted oceanic crust recycled into the Earth's deep interior and ultimately incorporated as an inherent component in the deep-seated mantle plumes is often considered to be responsible for the chemical and lithological heterogeneity in the source of OIBs (Hofmann, 1997; White, 2010). Incompatible trace elements are very sensitive to melting and differentiation processes, but are not good indicators of variable source mineralogy or lithology (e.g., Hofmann, 1997). Heavy radiogenic isotopes, on the other hand, can track mantle chemical heterogeneity but do not necessarily provide information of the mantle source lithology (e.g., recycled crust in the mantle may be present in the form of distinct pyroxenitic lithologies, but may also be expressed as

---

* Corresponding authors.
E-mail addresses: xurong@mail.gyig.ac.cn (R. Xu), liming19820426@163.com (M. Li).

https://doi.org/10.1016/j.epsl.2023.118499
Received 2 April 2023; Received in revised form 27 October 2023; Accepted 11 November 2023
0012-821X/

refertilized/metasomatized peridotite). Major and minor element geochemistry of basalt and olivine phenocryst is frequently adopted as tracking tools to trace the presence of pyroxene- and garnet-rich lithologies (e.g., eclogite or garnet pyroxenite - for simplicity, we hereafter use the term "pyroxenite" to refer to olivine-deficient, pyroxene- and garnet-rich lithology) in the source (e.g., Herzberg, 2011; Lambart et al., 2013; Le Roux et al., 2011; Sobolev et al., 2005; Yang et al., 2019). However, several recent studies suggested that these tracers may be compromised by crustal processes (Gleeson and Gibson, 2019; Lang and Lambart, 2022 and references therein) or variation of melting conditions (Matzen et al., 2017; Xu et al., 2020a).

Non-traditional stable Fe isotopes have been established as a promising, alternative tool to identify pyroxene-rich lithologies in the mantle (Williams and Bizimis, 2014). In principle, equilibrium Fe isotope fractionation among different phases during both high-temperature igneous processes and sub-solidus mantle conditions depends on the valence state and the bonding environment (Sossi and O'Neill, 2017). Because high valent ferric Fe has small ionic radii, it will form short and strong Fe-O bonds that favor heavy Fe isotopes (Dauphas et al., 2014; Sossi and O'Neill, 2017). Consequently, it is expected that Fe^{3+}-deficient phases, such as olivine, possess lighter $\delta^{56}Fe$ values compared to the Fe^{3+}-bearing phases, such as pyroxenes (Macris et al., 2015; Sossi and O'Neill, 2017). During mantle melting, as Fe^{3+} is more incompatible than Fe^{2+} (Canil and O'Neill, 1996; Davis and Cottrell, 2021; Le Roux et al., 2015; Mallmann and O'Neill, 2009; McGuire et al., 1991), and because Fe^{3+}-bearing clinopyroxene contributes more to the melt component than other minerals (e.g., Mallik et al., 2021), partial melts usually have higher $\delta^{56}Fe$ than the residue (Williams and Bizimis, 2014). As a result, both larger Fe isotopic fractionations between the partial melt and the residual mineral assemblage during melting of pyroxene-rich mantle and the inherent higher $\delta^{56}Fe$ nature of pyroxenite component compared to the olivine-rich peridotite are expected to cause pyroxenite-derived partial melts to have higher $\delta^{56}Fe$ than those derived from peridotite (Williams and Bizimis, 2014). Several recent Fe isotope studies on both OIBs and MORBs supported the role played by melting of pyroxenite lithologies in basaltic magma genesis (e.g., Gleeson et al., 2020; Guo et al., 2023a; Konter et al., 2016; Liao et al., 2021; Nebel et al., 2019; Shi et al., 2022; Soderman et al., 2021, 2022; Sun et al., 2020; Wang et al., 2021).

Continental intraplate alkali basalts share many common features with alkali OIBs, such as low silica contents and enriched incompatible trace element and radiogenic isotope compositions (e.g., Pilet, 2015; Xu et al., 2022, 2020b). Studies on bulk-rock and olivine phenocryst compositions indicated that mantle sources of many continental intraplate basalts could also contain pyroxenitic lithologies (e.g., Dai et al., 2019; Li et al., 2016; Xu et al., 2017; Yang et al., 2016; Yang and Zhou, 2013; Zou et al., 2022). However, limited data are available hitherto (Guo et al., 2023b; He et al., 2019; Shi et al., 2023). He et al. (2019) reported data that systematically investigate the Fe isotope behavior for continental intraplate basalts. In their study, the authors presented $\delta^{56}Fe$ values up to 0.29 for continental intraplate basalts from eastern China, approaching the higher end values observed for OIBs (Konter et al., 2016; Soderman et al., 2021). They attributed this heavy Fe signature to melting of a peridotite source, previously oxidized by recycled carbonates. Therefore, an apparent knowledge gap still exists between the heavy Fe isotope signatures of continental intraplate basalts and the plenty geochemical evidence for pyroxenitic lithologies in their mantle sources. It is this disconnect between theoretical expectations and observational data that motivates our reinvestigation of Fe isotope systematics of continental intraplate basalts.

Here, we report Fe isotope analyses performed on a suite of continental intraplate basalts from SE China, south of the area covered by He et al. (2019). These basalts were previously characterized for their Sr-Nd-Zn isotopic ratios and their major and trace element compositions (Xu et al., 2022). Providing iron isotopic analyses of these well-characterized samples gives a unique opportunity to test for the presence of lithological heterogeneity in the mantle source of continental intraplate basalts. Below, we demonstrate that the co-variations of Fe isotopes with the other geochemical and petrological parameters are the direct testimony in favor of interactions between a lithological heterogenous asthenosphere and the overlying mantle lithosphere, and we discuss the potential of the Fe-Zn isotopic system as a novel and promising tool for tracing the nature of the components in the mantle source of continental intraplate basalts.

2. Geological background and samples

Cenozoic intraplate alkali basaltic volcanism is widespread in eastern China (Xu et al., 2020b, 2018), mostly along the trans-lithospheric faults. The Cenozoic Zhejiang basalts are located in the northeastern South China block (Ho et al., 2003). In brief, the samples studied here are basanites, alkali basalts and minor tholeiites (< ~11Ma) from Xinchang (XC), Shengzhou (SZ) and Tiantai (TT) in the coastal area, and nephelinites and basanites (~26–17 Ma) from Xilong (XL) and Longyou (LY) in the inland area (Ho et al., 2003; Xu et al., 2022). Their detailed petrology, major and trace element contents and Zn-Sr-Nd isotopic compositions are reported in Xu et al. (2022). Here we provide a brief comparison between the early- and late-stage magmatism: the early-stage inland basalts have, in general, (1) higher MgO and total alkali (Na_2O+K_2O) contents and CaO/Al_2O_3 ratios and lower SiO_2 contents, (2) higher incompatible trace element contents (e.g., Sr and LREE), (3) higher ratios of more to less incompatible elements (e.g., Dy/Yb and Nb/Y), (4) higher ratios of elements with similar bulk partition coefficients (e.g., Ti/Eu), and (5) lower ratios of fluid-mobile to less fluid-mobile elements (e.g., K/La and Sr/Ce). Finally, the early-stage basalts show a coupled Zn-Sr-Nd isotopic composition with high $\delta^{66}Zn$ and moderately enriched Sr-Nd isotopic signals, whereas the late-stage basalts display a decoupled Zn-Sr-Nd isotopic signature with a pronounced $\delta^{66}Zn$ decrease with increasing SiO_2 and Sr isotope ratio and with decreasing alkalis and Nd isotope ratio.

3. Analytical methods

Iron isotopic analyses were conducted at the State Key Laboratory of Geological Processes and Mineral Resources, China University of Geosciences (Wuhan), utilizing established protocols by Lei et al. (2022). The sample powders which contain 50–100 μg Fe were weighed into 7 mL Savillex beakers. Sample powders were dissolved using double-distilled concentrated HF + HNO_3 (1:1), HNO_3 + HCl (1:3) by heating at 120℃ on a hotplate for 24 and 12 h, respectively. Dissolved samples were evaporated to dryness, then re-dissolved in 1 mL concentrated HCl and heated to dryness. Finally, solutions were dried and then dissolved in 0.5 mL 8 mol L^{-1} HCl (+0.001% H_2O_2) in preparation for column chemistry. The sample solutions were loaded onto 0.8 ml pre-cleaned AG-MP-1 M anion exchange resin to separate Fe from the matrix. The detailed exchange procedures of column chemistry are in Lei et al. (2022). The total procedural Fe blank is ~20 ng, which is negligible for analysis.

Iron isotopic measurements were performed on a Nu Plasma 1700 MC-ICP-MS (Nu Instruments, Wrexham, UK). Five μg g^{-1} Fe solutions produced a typical signal intensity of ~25 V for ^{56}Fe. The dissolved IRMM-014 Fe isotope standard with five μg g^{-1} Fe was used as the bracketing standard, and sample solutions were typically diluted to 5.00 ± 0.25 μg g^{-1} Fe for analysis. Iron isotopic compositions were reported using the standard per mil (‰) notation of $\delta^{56}Fe$ for $^{56}Fe/^{54}Fe$ ratio, and $\delta^{57}Fe$ for $^{57}Fe/^{54}Fe$ ratio, where:

$$\delta^{56}Fe = \left[\left(^{56}Fe/^{54}Fe_{sample}\right)\Big/\left(^{56}Fe/^{54}Fe_{IRMM-014}\right) - 1\right] \times 1000$$

$$\delta^{57}Fe = \left[\left(^{57}Fe/^{54}Fe_{sample}\right)\Big/\left(^{57}Fe/^{54}Fe_{IRMM-014}\right) - 1\right] \times 1000$$

To ensure reliability and comparability of our Fe isotope data, the reference materials BCR-2, BHVO-2, GSP-2 and AGV-2 were also analyzed (Table 1). Full details about the Fe elemental purification and isotope analysis can be found in Lei et al. (2022).

4. Results

The stable Fe isotopic compositions of the studied basalts and standard reference materials are provided in Table 1. The samples plot on the mass fractionation line in δ^{56}Fe vs. δ^{57}Fe space (Fig. S1) with a slope of 1.4942 ($R^2 = 0.9927$; $n = 55$), indicating negligeable or no analytical artifacts from unresolved isobaric interferences on measured Fe isotopic compositions. The measured δ^{56}Fe of the Zhejiang basalts ranges from 0.09‰ to 0.20‰, which expands to higher values than those published for MORB (δ^{56}Fe ranges from +0.07‰ to +0.14‰ with an average of +0.105‰ ± 0.006‰) (Teng et al., 2013). In general, the low-silica basalts have slightly higher δ^{56}Fe values (0.15 to 0.20‰ with an average of 0.16‰; $n = 8$) than the high-silica samples (0.09 to 0.19‰ with an average of 0.13‰; $n = 16$). δ^{56}Fe in the samples also shows broad correlations with SiO_2, elemental ratios and isotopic ratios (Figs.1-3).

5. Discussion

5.1. *Effect of crustal contamination and fractional crystallization*

Two of the analyzed samples (i.e., those with the highest SiO_2 contents) have been identified by Xu et al. (2022) as likely affected by crustal contamination: they have significantly higher Sr and lower Nd isotopic ratios than samples from the same locality (Shengzhou), and have the lowest Ce/Pb and Nb/U ratios than the other samples. These samples are not taken into account in the following discussion and are plotted as open symbols. For all the other samples, Xu et al. (2022) demonstrated that the effect of crustal contamination is negligeable.

Table 1

Iron isotopic compositions of the studied basalts and standard materials.

Sample	Location	δ^{56}Fe[a]	2SE[b]	δ^{57}Fe[a]	2SE[b]	$\delta^{56}Fe_{prim}$[c]	n[d]
18LY01	Longyou	0.15	0.01	0.23	0.05	0.15	3
18LY02	Longyou	0.16	0.03	0.26	0.03	0.15	3
18LY03	Longyou	0.16	0.02	0.23	0.02	0.14	3
18XL01	Xilong	0.20	0.01	0.30	0.04	0.19	3
18XL02	Xilong	0.20	0.01	0.30	0.04	0.18	3
18XL09	Xilong	0.15	0.01	0.22	0.02	0.14	3
18XL10	Xilong	0.15	0.03	0.23	0.01	0.14	2
18XL11	Xilong	0.16	0.03	0.26	0.02	0.15	3
18XC01	Xinchang	0.11	0.01	0.16	0.02	0.09	6
18XC03	Xinchang	0.11	0.02	0.13	0.01	0.09	2
18XC05	Xinchang	0.12	0.02	0.16	0.05	0.09	3
18XC15	Xinchang	0.12	0.01	0.21	0.04	0.10	3
18XC16	Xinchang	0.09	0.02	0.15	0.01	0.06	3
18TT01	Tiantai	0.15	0.02	0.21	0.02	0.13	3
18TT02	Tiantai	0.13	0.01	0.20	0.01	0.11	2
18TT03	Tiantai	0.11	0.02	0.17	0.03	0.09	3
18TT12	Tiantai	0.12	0.02	0.17	0.03	0.12	3
18TT13	Tiantai	0.18	0.02	0.22	0.05	0.17	2
18SZ10	Shenzhou	0.15	0.01	0.25	0.01	0.13	3
18SZ12	Shenzhou	0.17	0.02	0.23	0.04	0.16	3
18SZ13	Shenzhou	0.19	0.02	0.31	0.01	0.17	3
18SZ14	Shenzhou	0.14	0.02	0.22	0.04	0.12	3
18SZ18	Shenzhou	0.12	0.02	0.19	0.03	0.10	3
18SZ19	Shenzhou	0.11	0.02	0.18	0.02	0.08	3
BHVO-2		0.10	0.01	0.15	0.01		57
BCR-2		0.08	0.01	0.12	0.01		62
GSP-2		0.12	0.01	0.20	0.02		15
AGV-2		0.11	0.02	0.16	0.04		6

[a] δ^{56}Fe and δ^{57}Fe are permil deviation of the $^{56}Fe/^{54}Fe$ and $^{57}Fe/^{54}Fe$ ratio from the IRMM-014 standard.

[b] Two times standard error calculated as $2SE = 2SD/n^{1/2}$ with SD represents standard deviation.

[c] $\delta^{56}Fe_{prim}$ represent olivine fractionation-corrected values.

[d] n represents the times of repeat measurements of the same purified solution by MC-ICP-MS.

Crystal fractionation during magma petrogenesis is known to affect the original Fe isotope composition of the ascending magma, it is therefore important to assess its potential role in the Fe isotope evolution of our studied basalts. The samples studied here that not affected by crust assimilation have > ~8 wt.% MgO and < ~48.5 wt.% SiO_2 and no signs of clinopyroxene fractionation was observed (e.g., the positive correlation between clinopyroxene fractionation-sensitive elements, such as *Sc* and magma evolution indices, such as SiO_2, argues against significant clinopyroxene fractionation; see also in Xu et al., 2022), indicating these basalts have not fractionated any phases other than olivine. Overall, fractional crystallization of magmatic olivine preferentially incorporates isotopically light Fe, enriching the evolved melt in heavy Fe isotopes (Teng et al., 2008). To evaluate the Fe isotope composition of primary magmas, we correct the effect of olivine removal on δ^{56}Fe values following the scheme of Sossi et al. (2016). In the correction, we use an olivine-melt Fe-Mg exchange partition coefficient ($K_D^{Fe\text{-}Mg}$) of 0.32, and iteratively add equilibrium olivine by 0.01 increment into the melt until the melt ($Mg^{\#} = 74$) is in equilibrium with a mantle olivine of Fo_{90}. We assume an initial $Fe^{3+}/\Sigma Fe$ ratio of 0.15 (Xu et al., 2022) and use an isotope fractionation factor $\Delta^{56}Fe_{olivine\text{-}melt} \sim \frac{2853\times(\langle F\rangle_{olivine}-\langle F\rangle_{melt})}{T^2}$ after Dauphas et al. (2014), where $\langle F\rangle$ is the mean force constant of Fe-O bonds ($\langle F\rangle_{olivine}$ ~197 N/m, $\langle F\rangle_{Fe^{2+},\ melt}$ ~199 N/m, $\langle F\rangle_{Fe^{3+},\ melt}$ ~351 N/m and $\langle F\rangle_{melt} = (1 - Fe^{3+}/\sum Fe) \times \langle F\rangle_{Fe^{2+},\ melt} + Fe^{3+}/\sum Fe \times \langle F\rangle_{Fe^{3+},\ melt}$), and T (temperature) in Kelvin is calculated similarly to that of Sossi et al. (2016). The corrected δ^{56}Fe values range from +0.06 to 0.19‰ and are only slightly lower than the measured values (Table 1). The validity of our correction scheme is supported by the negative correlation between Δ^{56}Fe ($= \delta^{56}Fe_{measured} - \delta^{56}Fe_{primary}$) and Ni content (Fig. S2), as Ni is an independent marker of olivine fractionation and thus not affected by our correction.

In the following sections, we will use the corrected δ^{56}Fe values (Figs. 1-6) to assess the Fe isotope variations of mantle sources/processes. We note however that the correlations described below, and their associated interpretations would stand if the measured δ^{56}Fe values were plotted instead.

5.2. *Effect of melting conditions of a peridotite mantle*

Both source heterogeneity and mantle process such as partial melting could produce Fe isotope variations in the primary magmas. Source heterogeneity is well-characterized in the studied samples. For instance, in the Sr-Nd isotopic space, three isotopically different components can be identified for these samples, anchoring a distribution of compositions among a depleted mantle endmember, a carbonated-pyroxenite and a subduction-modified SCLM (Xu et al., 2022). These heterogeneous source components may have distinct mineral assemblages and/or Fe isotope compositions, thus may be responsible for the observed Fe isotope heterogeneity. However, before this assertion we need to evaluate the effect of melting conditions (melting degree, mantle redox state, source mineralogy and mantle potential temperature) that may have on the δ^{56}Fe of our samples.

Overall, the early-stage basalts (LY and XL) have slightly higher and less variable δ^{56}Fe values than the late-stage samples (XC, TT and SZ) (Figs. 1-2). Both the Fe isotopic variation and the heavy Fe isotope compositions could be the result of partial melting process (Gleeson et al., 2020; Williams and Bizimis, 2014). To explore whether partial melting of mantle peridotite and/or variation of the mantle source fO_2 can generate the observed heaviest Fe isotope signatures, we quantitatively investigate Fe isotope fractionation during adiabatic decompression (Fig. 4). We used the phase assemblages along adiabatic decompression paths for mantle potential temperatures (Tp) of 1300 °C and 1550 °C determined by Elkins et al. (2019) for melting of pure peridotite with the BSE-type Fe isotope composition (δ^{56}Fe = 0.02 ± 0.03‰, Weyer and Ionov, 2007) and used the same approach to

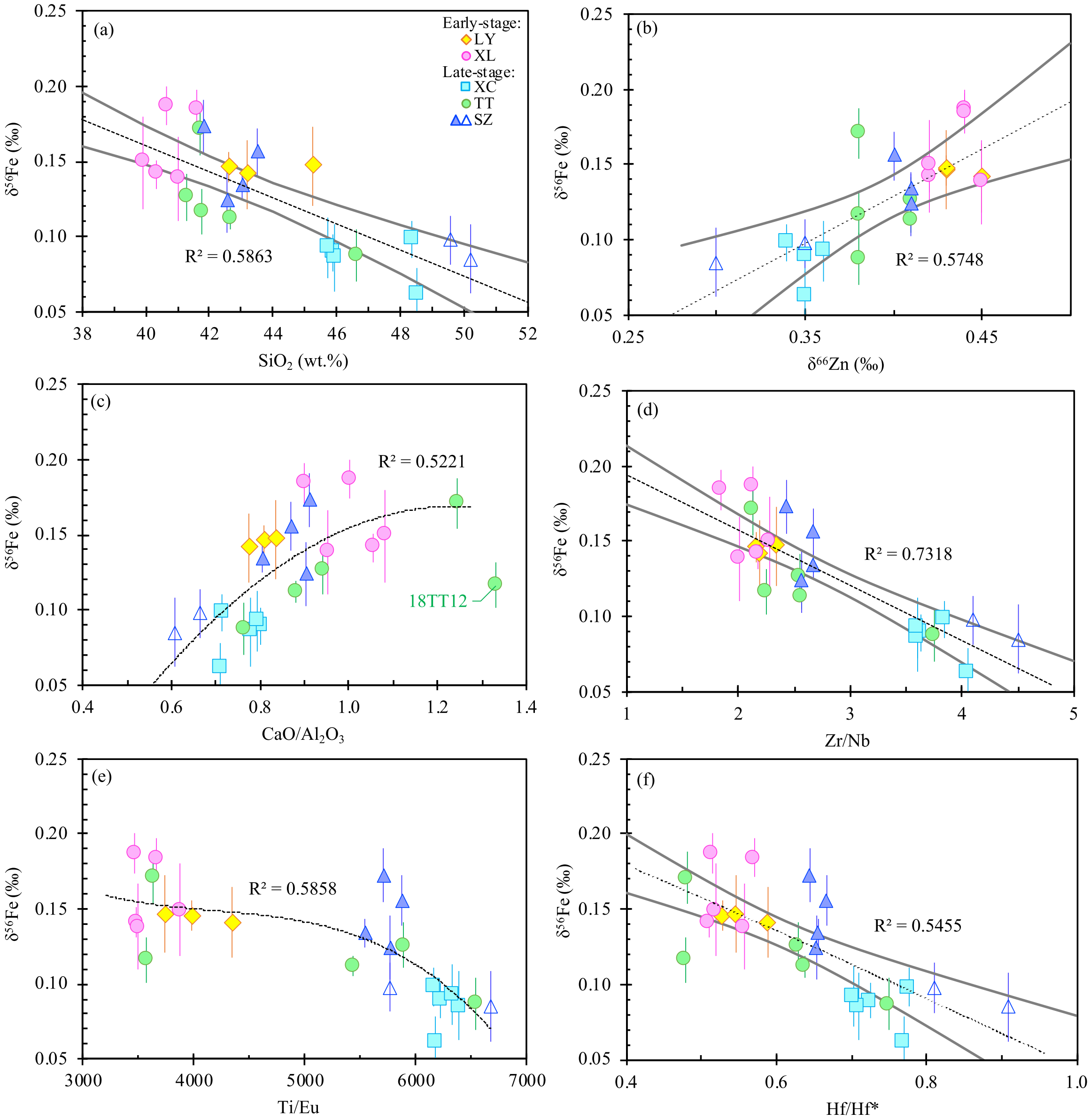

Fig. 1. Fractionation-corrected δ^{56}Fe variation as a function of SiO_2, δ^{66}Zn, CaO/Al_2O_3, Zr/Nb, Ti/Eu and Hf/Hf* (Hf anomaly). The best-fit regressions with R^2 values are shown, with the 95% confidence intervals for these regressions. The error bars represent 2 S.E., and are calculated as follows: 2 S.E. = 2 S.D. / $n^{1/2}$, with n being the number of analyses.

calculate the mineral mode evolution at Tp = 1400 °C (Fig. S3): the pressure-temperature-melt fraction paths are determined using Melt-PX (Lambart et al., 2016) and the corresponding phase assemblages are determined with pMELTS (Ghiorso et al., 2002). The method is described in detail in Elkins et al. (2019). Accumulated melt and residue compositions (i.e., FeO, Fe_2O_3, Dy and Yb concentrations and δ^{56}Fe) are calculated using an incremental (dP = 0.1 kbar) non-modal melting model (Williams and Bizimis, 2014). To account for the effect of $Fe^{3+}/\Sigma Fe$ on the melt δ^{56}Fe, we estimate the force constants for the Fe-O bonds for mineral sites hosting Fe in olivine (ol), orthopyroxene (opx), clinopyroxene (cpx), spinel (sp) and garnet (gt) using equations in Sossi and O'Neill (2017) and the force constant estimated for basaltic melts by the Nuclear Resonant Inelastic X-ray Scattering in Dauphas et al. (2014). We also test for the effect of oxygen fugacity by varying the mineral $Fe^{3+}/\Sigma Fe$ and the partition coefficients for Fe^{3+} and Fe^{2+} to cover a large range of fO_2 (equivalent to ~ FMQ (fayalite-magnetite-quartz) −2.85 to FMQ + 3.01). In parallel with the decompression melting calculations, we also performed another set of model calculations (Fig. 5) considering isobaric melting of a peridotite at both low-pressure (1.5 GPa) spinel stability field and high-pressure (3–7 GPa) garnet stability field, with the solidus mineral modes and pressure-dependent melt reactions calculated according to the experimental parameterization of Brown and Lesher (2016). The parameters used in the calculations are reported in Table 2 and Tables S1 and S2. Our decompression and isobaric melting models show that:

(1) the magnitude of Fe isotope fractionation during partial melting of peridotite (Δ^{56}Fe) is relatively small and lower than 0.04–0.05‰, independently of the mantle fO_2 and Tp (Figs. 4 and 5). This is consistent with previous estimates (Gleeson et al., 2020; Shi et al., 2022; Soderman et al., 2021; Sossi and O'Neill, 2017).

(2) while increasing the potential temperature from 1300 to 1400 °C slightly increases the fractionation of δ^{56}Fe of the low degree melts because of the appearance of garnet in the residue (Fig. S3), further increase of the potential temperature (and of the pressure

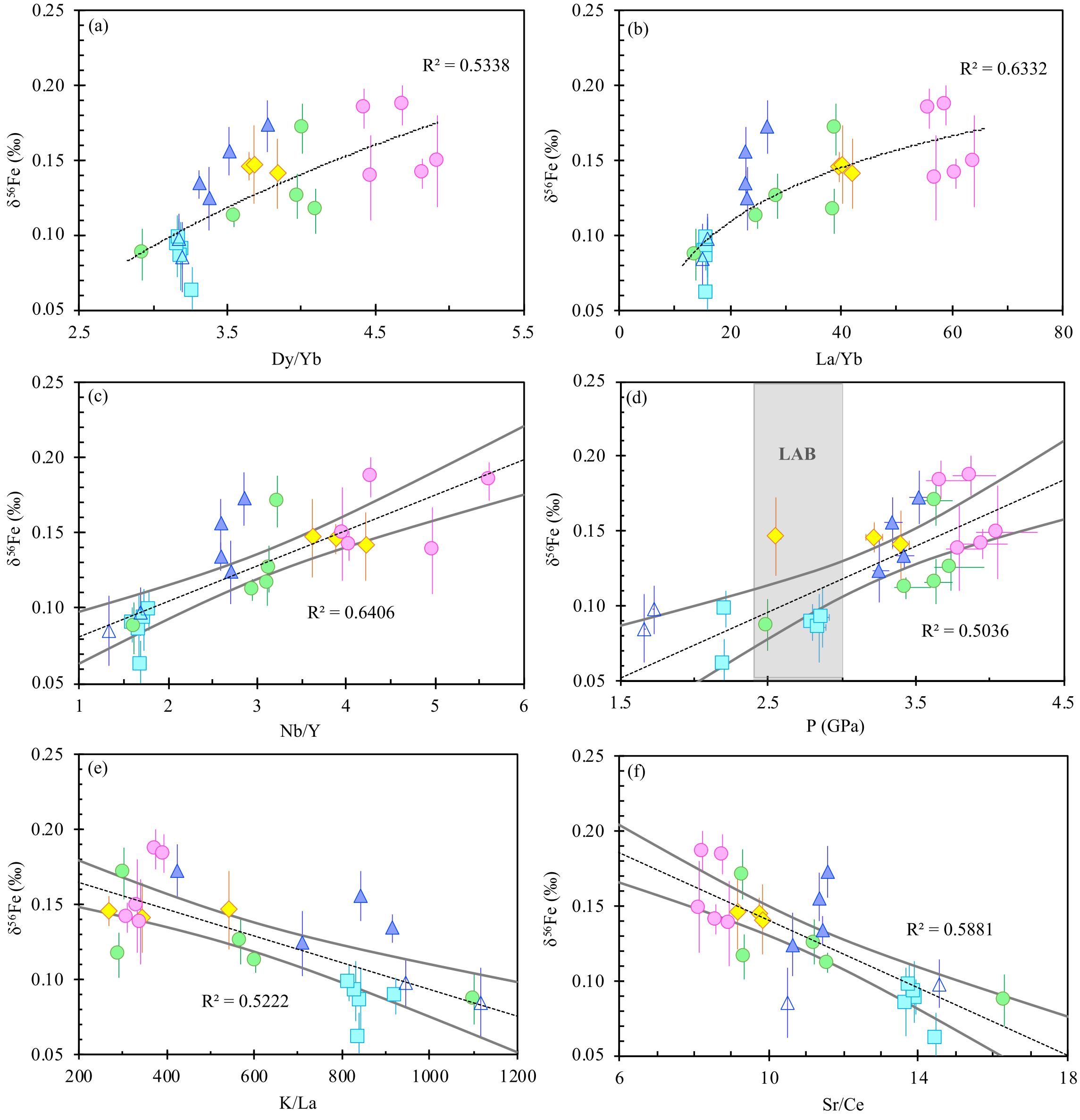

Fig. 2. Fractionation-corrected δ^{56}Fe variation as a function of Dy/Yb, La/Yb, Nb/Y, P (equilibrium pressure of segregation, details of calculation can be found in Xu et al., 2022), K/La and Sr/Ce. The best-fit regressions with R^2 values are shown, with the 95% confidence intervals for regressions. Symbols and error bars are as in Fig. 1.

of melting) results in similar or lower δ^{56}Fe in low-degree partial melts (Figs. 4). In fact, although the solidus mode of garnet slightly increases with Tp, partial melt produced at higher pressure are produced from a higher consumption of olivine which leads to an enrichment of the partial melts in light Fe isotope. This is also supported by the isobaric melting model results which show that both higher melting temperatures and more consumption of olivine and garnet with low δ^{56}Fe at higher pressures will lead to partial melts enriched in lighter Fe isotope (Fig. 5). The observed correlations between δ^{56}Fe and Dy/Yb (Figs. 6 and S4) and estimated segregation pressures (Fig. 2d) therefore do not imply a causal relationship between the abundance of residual garnet in the peridotite mantle source and the Fe isotope composition of continental intraplate basalts.

(3) variations of the melting conditions of a peridotite mantle alone cannot explain the variability of δ^{56}Fe observed in our study (Figs. 4 and 5). For an intermediate fO_2, close to FMQ, the maximal fractionation is observed for Tp = 1400 °C. At this mantle potential temperature, low degree partial melt of a highly oxidized mantle source reaches δ^{56}Fe values up to 0.07‰. In our study, however, all but one samples have $\delta^{56}Fe_{primary} > 0.07$‰ (Table 1).

In summary, partial melting of a peridotite mantle cannot explain the high δ^{56}Fe values of our samples; this latter most likely reflects a lithological heterogeneity.

5.3. Fe-Zn isotopic pair: a tracer for the mantle components

5.3.1. A 3-component mantle source

He et al. (2019) suggested that the component responsible for the high δ^{56}Fe observed in Cenozoic basalt from eastern China is a peridotitic source metasomatized and oxidized by recycled carbonates. In fact, some metasomatized peridotite record high δ^{56}Fe, up to 0.17‰ (Weyer and Ionov, 2007) and may produce a possible melt end-member with heavier Fe isotope composition that would explain the variability of our samples. This is consistent with many compositional features of our early-stage basalts (e.g., low silica contents, low Ti/Eu and K/La, negative Hf anomalies, high δ^{66}Zn; Figs. 1 and 2) that indicate that a carbonatite melt (see Xu et al., 2022 for details) rather than a low-degree melt sourced from normal depleted MORB-like asthenosphere (Guo et al., 2023a, 2023b; Sun et al., 2020), must be involved in their generation. However, the iron isotopic signatures reported for suites of xenoliths from Cameroon and Kergelen, both interpreted as metasomatized by carbonated-mafic melts, mostly expand toward low δ^{56}Fe values (down to −0.153‰ with a mean value of −0.078‰ and down to −0.54‰ with a mean value of −0.03‰, respectively; Poitrasson et al., 2013). In addition, Johnson et al. (2009) showed that a carbonatite melt in equilibrium with the silicate mantle is expected to have negative δ^{56}Fe values (< −0.3‰). Hence, if a carbonatite melt acts as a metasomatic agent here, it would result in decreasing the δ^{56}Fe values of the peridotite. Therefore, carbonated peridotite is not a good candidate for the high δ^{56}Fe. As described in Section 5.2, the oxidation of the source alone also cannot explain the heaviest iron isotopic compositions observed in the basalts.

Pyroxenite are known to have heavier iron isotopic signatures (Williams and Bizimis, 2014). In addition, the basalts with the highest δ^{56}Fe also have some of the highest δ^{66}Zn values (Fig. 1). Xu et al. (2022) demonstrated that the heavy Zn isotopic signature of the low-silica basalts along with their major and trace element features indicates the presence of a carbonated component in the mantle source. Hence, the best candidate for the isotopically heavy endmember appears to be a carbonated pyroxenite. The compositional variability of the heavy early-stage basalts is then consistent with melting of both the carbonated pyroxenite and the surrounding peridotite.

Late-stage basalts also partly record the mantle upwelling. In fact, progressive melting of a lithologically heterogeneous asthenosphere will result in the signal from the pyroxenite to be increasingly diluted and thus in a decrease of the melt δ^{56}Fe. However, the basalts with the lightest iron signature also have the most enriched Sr-Nd isotope compositions (Fig. 3), which is not consistent with an increasing contribution of the depleted peridotitic mantle. This interpretation also fails to explain why the late-stage basalts have significantly higher K/La and Sr/Ce ratios, two ratios that do not fractionate during melting (Fig. 2). To explain the co-variations of Sr-Nd isotopic compositions and of the fluid mobile/immobile element ratios with depth (Figs. 2 and 3), Xu et al. (2022) suggested a contribution from the subcontinental lithospheric mantle (SCLM) modified by subducted silicious sediment component. Considering the low δ^{56}Fe values of our samples are found in magmas with equilibrium depths (calculated with the barometer of melt silica activity buffered by coexisting olivine-orthopyroxene with additional corrections for the effect of CO_2, see details in Xu et al., 2022) coinciding with or close to the lithosphere-asthenosphere boundary (LAB) (Fig. 2d), this would suggest that the melt generated by the SLCM under the Zhejiang area must have a lower δ^{56}Fe value than the asthenospheric mantle. The SCLM in the Zhejiang area is thought to have suffered from early melt depletion and subsequent subduction-related metasomatic processes (see references in Xu et al., 2022). Both influx of slab-derived fluids and prior melt extraction would result in a SCLM depleted in heavy iron isotopes (e.g., Nebel et al., 2013). This is also consistent with the light Fe isotope compositions reported in arc magmas that are interpreted as reflecting the contribution of a melt-depleted, refractory, low-δ^{56}Fe mantle wedge (Foden et al., 2018). Mixing of melts derived from the heterogeneous carbonated pyroxenite-bearing asthenosphere with low degree melt produced by the SCLM, previously modified by slab-derived fluids during fossil subduction, consequently might elucidate the origin of both the high and the low δ^{56}Fe values of continental intraplate basalts.

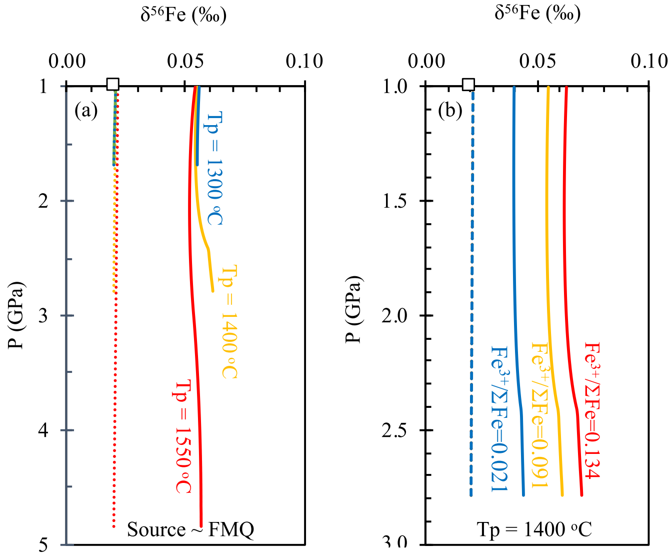

Fig. 4. δ^{56}Fe in the accumulated melt (solid line) and the residue (dashed line) for adiabatic melting of peridotite melting **(a)** at T_P = 1300 °C, 1400 °C and 1550 °C and for an intermediate oxidation of the source (~ FMQ), and **(b)** at T_P = 1400 °C and for a source Fe^{3+}/Fe^{total} of 0.021, 0.091, and 0.134 (equivalent to FMQ −2.85, FMQ+0.25 and FMQ + 3.01, respectively). The open square is the bulk composition of peridotite used in the calculation with δ^{56}Fe = 0.02 ± 0.03‰ (Weyer and Ionov, 2007). Details of the calculations can be found in the main text; the phase assemblage evolutions are presented in Fig. S3 and the parameters used in calculations are compiled in Table 2.

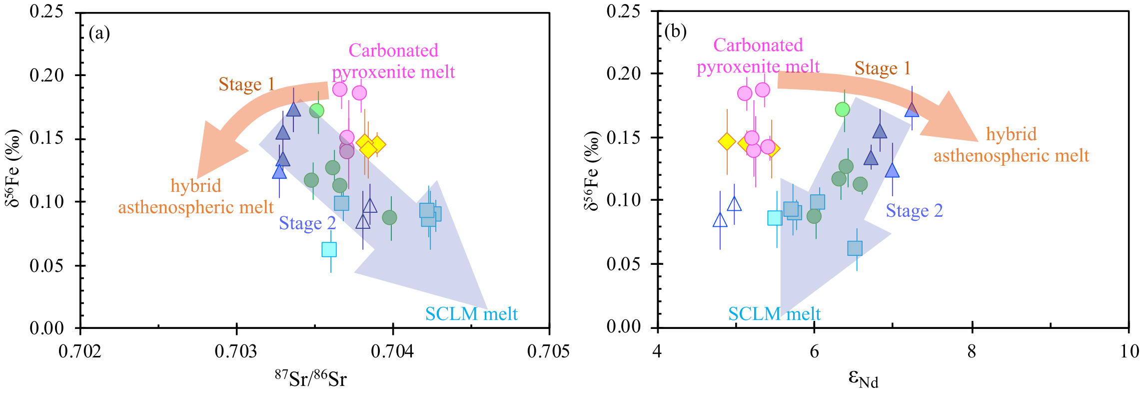

Fig. 3. Variation of fractionation-corrected δ^{56}Fe as a function of $^{87}Sr/^{86}Sr$ and ε_{Nd} for the studied basalts. The stage 1 arrow indicates decompression melting of the heterogeneous asthenosphere that dilutes the enriched signature of carbonated pyroxenite. The stage 2 arrow indicates mixing of melt from subduction-modified SCLM with the hybrid asthenospheric melt. See details in the main text.

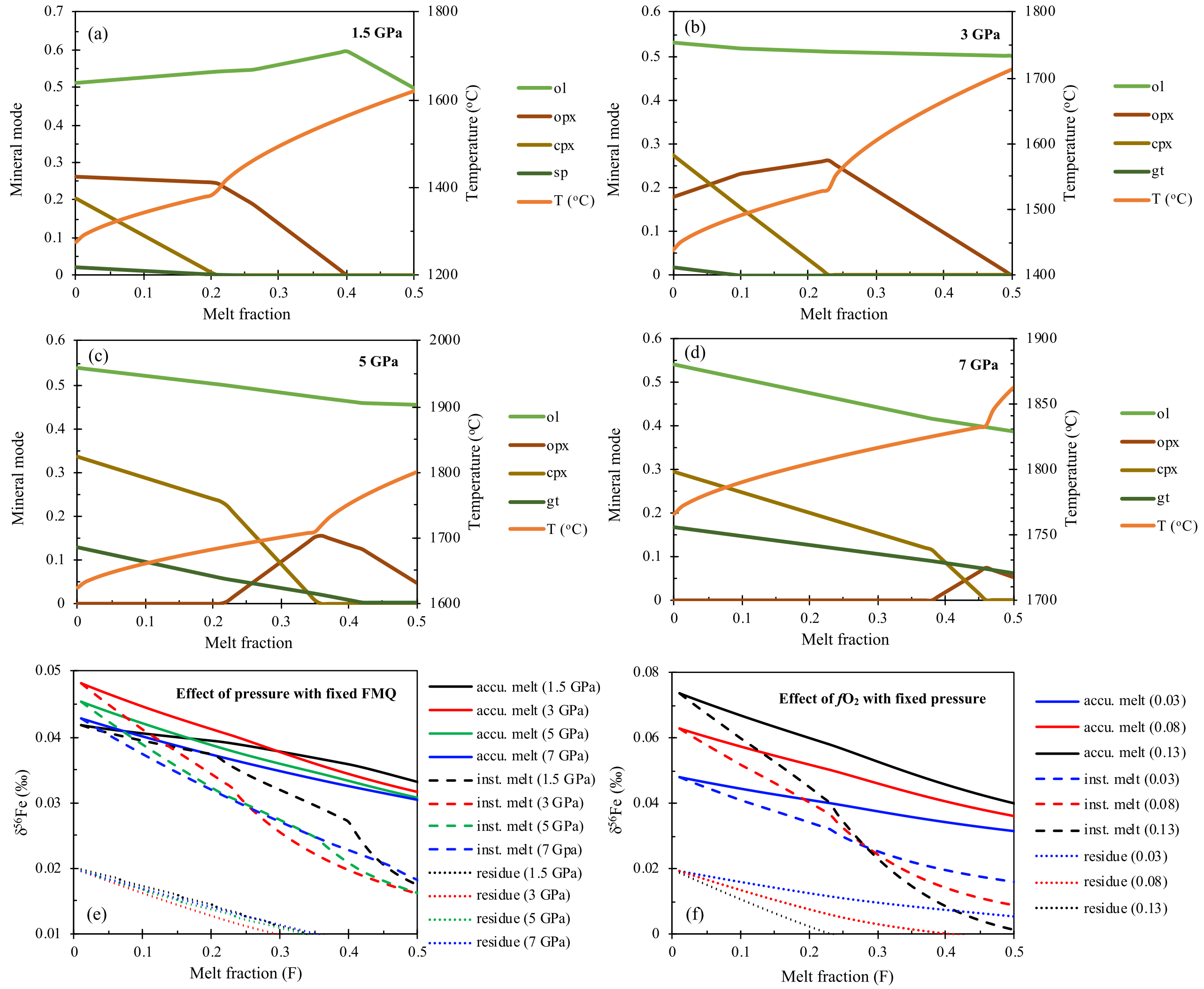

Fig. 5. (a-d) Phase proportions and melting temperatures during isobaric incremental non-modal melting of peridotite at four different pressures (1.5, 3, 5 and 7 GPa). (e) δ^{56}Fe in instantaneous (inst. melt) and accumulated (accu. melt) melt and residue for peridotite melting at the different pressures. (f) δ^{56}Fe in instantaneous and accumulated melt and residue melting of garnet peridotite at 3 GPa with different source Fe^{3+}/Fe^{total} of 0.03, 0.08 and 0.13, respectively. The initial peridotite $\delta^{56}Fe = 0.02$ (Weyer and Ionov, 2007). The solidus mineral mode and pressure-temperature-dependent melting reactions are calculated according to Brown and Lesher (2016). Parameters used in the calculations are reported in Tables 2, S1 and S2.

Table 2

Parameters used for modeling iron isotope fractionation during partial melting (Fig. 4).

	olivine	opx	cpx	spinel	garnet	melt
$D^{F2+}_{min\text{-}melt}$[a]	1.06	0.69	0.71	0.95	0.654	
$D^{F3+}_{min\text{-}melt}$	0.063[b]	0.63[c]	0.78[c]	$f(T,[Fe_2O_3]_{sp})$[c]	0.18[b]	
$Fe^{3+}/\sum Fe$ reduced	0.01[d]	0.03[c]	0.07[c]	0.064[c]	0.02[e]	
$Fe^{3+}/\sum Fe$ intermediate	0.035[d]	0.19[c]	0.32[c]	0.25[c]	0.075[e]	
$Fe^{3+}/\sum Fe$ oxidized	0.06[d]	0.28[c]	0.41[c]	0.639[c]	0.13[e]	
$K_{Fe\text{-}O}$	$185 + 125(Fe^{3+}/\sum Fe)$[b]	$185 + 125(Fe^{3+}/\sum Fe)$[b]	$185 + 125(Fe^{3+}/\sum Fe)$[b]	$225 + 125(Fe^{3+}/\sum Fe)$[b]	$145 + 125(Fe^{3+}/\sum Fe)$[b]	$199 + 152(Fe^{3+}/\sum Fe)$[f]
FeO_T (wt.%)	9.5[b]	7[b]	5[b]	15[g]	7[b]	

[a] Le Roux et al., 2015.

[b] Sossi and O’Neill, 2017.

[c] Davis and Cottrell, 2021 with $\ln[DFe^{3+}sp\text{-}melt] = 0.87\times10{,}000/T(K)-4.6 + 0.24*\ln([Fe_2O_3]sp\ (wt.\%))$, and $Fe^{3+}/\sum Fe$ reduced, intermediate and oxidized corresponding to ratios determined in experiments at FMQ-2.85, FMQ+0.25 and FMQ + 3.01, respectively.

[d] McGuire et al., 1991, the intermediate $Fe^{3+}/\sum Fe$ is the average between the minimal and the maximal value.

[e] Canil and O’Neill, 1996, the intermediate $Fe^{3+}/\sum Fe$ is the average between the minimal and the maximal value.

[f] Dauphas et al. (2014).

[g] Williams and Bizimis, 2014

5.3.2. A two-stage melting process

To test the hypothesis of the contribution of three distinct mantle components in the genesis of the basalt suite, we model the mixing of melt produced from peridotite and carbonated pyroxenite along an adiabatic decompression path for Tp = 1400 °C (i.e., the average Tp estimated for the Zhejiang basalts, Xu et al., 2022), with a final pressure of 2.5 GPa, and an intermediate source $Fe^{3+}/\Sigma Fe$ (Table 2). To calculate the mineral assemblages of the carbonated pyroxenite along the decompression path, we apply the approach used for decompression peridotite melting (Section 5.2), but for a bulk composition corresponding to mixing 7% magnesium carbonatite (80LI34, Hoernle et al., 2002) with pyroxenite (MIX1G, Hirschmann et al., 2003). There is no melting parameterization that exists to model the melting of a carbonated pyroxenite, so we run calculations assuming volatile-free lithologies. Despite this caveat, the addition of CO_2 to the pyroxenite will mostly depress its solidus (i.e., the pyroxenite will start to melt at higher pressure, e.g., Gerbode and Dasgupta, 2010), but is unlikely to strongly affect the melt productivity of the pyroxenite because of the “low-tail effect”. In other words, the melt fraction produced along the adiabatic path between the carbonated solidus and the anhydrous solidus would stay small. Model calculations show that mixing of carbonated pyroxenite melts and peridotite melts along an adiabatic path can generate both the heavy iron isotopic signature and the high Dy/Yb ratios (Fig. 6). To limit the scope of this study, we used fixed values for the δ^{56}Fe of the peridotite and the pyroxenite component in the asthenosphere. As discussed above, the peridotite component might have an iron isotopic composition that diverges from BSE, with potentially a higher value for δ^{56}Fe than considered in these calculations. Similarly, the (carbonated) pyroxenite component might have an iron isotopic composition that differs from the garnet pyroxenite considered in Williams and Bizimis (2014). From Fig. 6a, we can easily predict that using a heavier iron isotopic composition for the peridotite component and a lighter composition for the carbonated pyroxenite component would result in a narrower range of δ^{56}Fe values produced by the melting of a heterogeneous asthenospheric mantle; so changing the initial isotopic compositions would mostly affect the respective contribution of each component in basalts, but would not change the main conclusion that a lithologically heterogeneous mantle is required to explain the scatter in δ^{56}Fe observed in the samples. We also note that using a CO_2-free pyroxenite composition in our calculations would not be able to produce the highest Dy/Yb ratios as carbonatites are usually significantly more enriched in REE and present much more fractionated REE pattern (i.e., higher Dy/Yb ratios) than MORB (e.g., Hoernle et al., 2002), which is consistent with the low silica contents, and the low Ti/Eu and K/La ratios observed in the early-stage basalts (Fig. 1). This is also in agreement with previous conclusions from Xu et al. (2022) who showed that a carbonated recycled component is indeed required to explain the high δ^{66}Zn and moderately radiogenic Sr-Nd isotope compositions of these samples.

To test for a contribution of the SCLM, we perform isobaric calculations using pMELTS (Ghiorso et al., 2002) at 2.5 GPa, simulating in-situ melting of the SCLM between $F = 1\%$ and 5%. For the SCLM, we used the DMM composition from (Workman and Hart, 2005) and we test for two initial values of δ^{56}Fe: 0.013‰ and −0.017‰ (Foden et al., 2018). The compositional variation of the SCLM-derived melt between $F = 1\%$ and 5% is negligible (less than 0.005‰) and our results show that mixing of hybrid melts produced by the heterogeneous carbonated pyroxenite-bearing asthenosphere (Stage 1) with low-degree melts from the SCLM (Stage 2) well account for the overall positive correlation between δ^{56}Fe and Dy/Yb ratios (Fig. 6). The relatively low Dy/Yb and high Lu/Hf ratios and the thermobarometer constraints indicate the low δ^{56}Fe sample melts from the lower SCLM or the LAB depth. This is also supported by their high K/La, Ba/Th and Sr/Nd ratios and their enriched Sr-Nd isotopic compositions, indicating there must be a substantial contribution from subduction-modified SCLM components to the low δ^{56}Fe samples.

All additional parameters used in these calculations are presented in Tables S1 and S2. Additionally, to test the effects of pressure and of the $Fe^{3+}/\Sigma Fe$ of the source minerals on our model, we performed another set of calculations considering isobaric melting at 3, 5 and 7 GPa and taking into account that spinel peridotite, garnet peridotite and pyroxenite likely do not have the same mineral chemistry (Table S2). These calculations show that our results are not model dependent: blending of

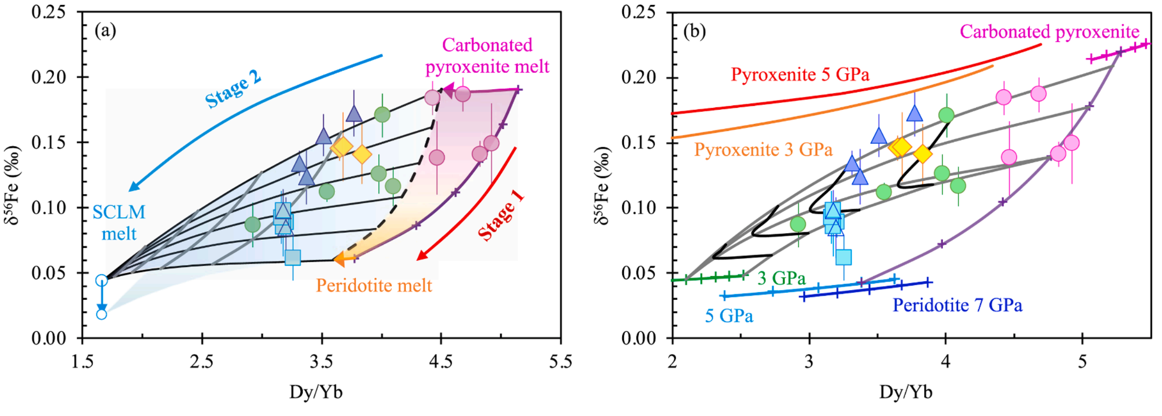

Fig. 6. Variation of fractionation-corrected δ^{56}Fe vs. Dy/Yb for the studied continental intraplate basalts compared with **(a)** the 2-stage adiabat decompression model and **(b)** isobaric melting model described in the text. In **(a)**, the pink-to-orange area represents melt compositions produced by decompression melting at T_P=1400 °C and for a final pressure of 2.5 GPa of a carbonated pyroxenite-bearing asthenosphere (Stage 1). The pink and orange arrows show the composition of carbonated pyroxenite melt and pure peridotite melt produced during the decompression. The shaded blue area represents mixing of hybrid melts produced in Stage 1 with melts produced by 5% melting of the SCLM at 2.5 GPa (Stage 2). The gray curves are isopleths of mixing fraction with each increment represents 0.2. The blue arrow linking two blue circles shows the effect of decreasing the SCLM δ^{56}Fe from 0.013‰ to −0.017‰ (Foden et al., 2018). All the parameters used to create this model are compiled in Table 2 and Table S1. In **(b)**, also shown are isobaric melting curves ($F = 1$ to 5% with each increment of 1%) for peridotite at 3 GPa (green line), 5 GPa (light blue line with $F = 1, 5, 10, 15, 20\%$) and 7 GPa (dark blue line with $F = 1, 5, 10, 15, 20\%$), for Mix1G pyroxenite at 3 GPa (orange line) and 5 GPa (red line) and for carbonated Mix1G pyroxenite at 5 GPa (pink line with $F = 1, 5, 10, 15, 20\%$). The purple line represents binary mixing of partial melts ($F = 5\%$) of garnet peridotite, with partial melts ($F = 10\%$) of carbonated pyroxenite at 5 GPa in the asthenosphere with each increment of 0.2. The gray lines represent mixing of hybrid melts derived from carbonated pyroxenite-bearing heterogeneous asthenosphere at 5 GPa with partial melts of the lower part of lithospheric mantle at 3 GPa. The black curves are isopleths of mixing fraction with each increment represents 0.2. For pyroxenite melting, the solidus mineral mode and pressure-temperature-dependent melting reactions are calculated for MIX1G according to Brown and Lesher (2016). All the parameters used to create this model are compiled in Table S2.

carbonated pyroxenite melt with peridotite melt at high pressure can generate melt with heavy iron isotopic signature and high Dy/Yb ratios that cannot be generated by peridotite melting, and mixing of these heavy hybrid melts with shallow melts of mantle peridotite reproduce the positive correlation between δ^{56}Fe and Dy/Yb ratios (Fig. 6).

5.4. *Global implications for the study of continental intraplate basalts*

Several studies have suggested that continental intraplate basalts contain recycled mafic crustal materials in their mantle sources (e.g., Dai et al., 2019; Hoernle et al., 2006; Li et al., 2016; McGee et al., 2015; Sakuyama et al., 2013; Timm et al., 2009; Xu et al., 2017, 2020b; Yang et al., 2016; Zou et al., 2022). Decompression melting of a heterogeneous asthenosphere has also been raised to explain the compositional variation of the silica-deficient continental alkaline mafic volcanic rocks. However, whether the source is dominated by carbonated peridotite (e.g., He et al., 2019; Liu et al., 2016; Zeng et al., 2010) or composed of diverse lithologies (e.g., peridotite + carbonated pyroxenite residing deep in the asthenosphere; Hoernle et al., 2006; Li et al., 2016; McGee et al., 2015; Sakuyama et al., 2013; Timm et al., 2009; Xu et al., 2020b, 2018) remains contentious. Similarly, both a silica-rich pyroxenite component (e.g., Li et al., 2016; Xu et al., 2018 and references therein) and the depleted lithospheric mantle (e.g., Timm et al., 2009; Xu et al., 2022) have been proposed as playing a role in the formation of high-silica continental intraplate basalts. Together with conventional major and trace elements and radiogenic isotopes, the iron-zinc stable isotope pair strikes as being a powerful tool to discriminate between the potential mantle components, with iron isotopes acting as a tracer of lithological heterogeneity, and zinc isotopes acting as a probe for the presence of carbonated lithology in the mantle source, and may consequently provide critical insights into the geodynamics for generation of continental intraplate basalts.

6. Conclusions

We present Fe isotope data for well-characterized Cenozoic continental intraplate basalts from SE China. This suite of basalts has been separated in two groups: early-stage inland samples with low-silica contents and enriched Zn-Sr-Nd isotopic signatures, and later-stage coastal basalts that show a pronounce δ^{66}Zn decrease with increasing SiO_2 and $^{87}Sr/^{86}Sr$ and with decreasing alkali contents and ε_{Nd}. Our results show that the Fe isotope values of these basalts are strongly correlated with the other compositional features, with the early-stage basalts exhibiting the highest δ^{56}Fe and the iron isotopic values of the suite displaying positive correlations with alkali content, δ^{66}Zn, CaO/Al_2O_3, ratios of more to less incompatible elements (e.g., La/Yb, Dy/Yb and Nb/Y) and ε_{Nd}, and negative correlations with SiO_2, ratios of fluid mobile/immobile element (K/La and Sr/Ce) and $^{87}Sr/^{86}Sr$.

Our study shows that iron isotope fractionation is limited during partial melting of peridotite, consistently with previous studies (e.g., William and Bizimis, 2014; Soderman et al., 2021), and demonstrates that neither the presence of residual garnet nor a high degree of oxidation of the source has a significant effect on the iron isotopic signature of the melt. On the contrary, our study supports the contribution of carbonated pyroxenitic lithologies is responsible for the heavy iron and zinc isotopic signatures and the low silica contents and Ti/Eu and K/La ratios, and shows that decompression melting of a carbonated pyroxenite-bearing asthenosphere can produce the high δ^{56}Fe and δ^{66}Zn values of the early-stage basalts. Subsequential progressively decompression melting and mixing with low-degree melts from the subduction-modified sub-continental lithospheric mantle can reproduce the compositional variability of the late-stage suite. We propose that Fe isotopes can be used as a powerful tool to identifying source lithology of continental intraplate basalts in future studies.

CRediT authorship contribution statement

Rong Xu: Conceptualization, Data curation, Formal analysis, Investigation, Methodology, Visualization, Writing – original draft, Writing – review & editing. **Sarah Lambart:** Investigation, Writing – review & editing. **Oliver Nebel:** Writing – review & editing. **Ming Li:** Funding acquisition, Writing – review & editing. **Zhongjie Bai:** Writing – review & editing. **Junbo Zhang:** Writing – review & editing. **Ganglan Zhang:** Writing – review & editing. **Jianfeng Gao:** Writing – review & editing. **Hong Zhong:** Writing – review & editing. **Yongsheng Liu:** Resources, Writing – review & editing.

Declaration of Competing Interest

The authors declare that they have no known competing financial interests or personal relationships that could have appeared to influence the work reported in this paper.

Data availability

Data used in this paper is included in Manuscript and Supplementary Information.

Acknowledgments

We appreciate Carrie Soderman and an anonymous reviewer, as well as the editor Rosemary Hickey-Vargas for thorough and helpful comments that greatly improved the quality of this manuscript. We also thank Eric Brown, Yangtao Zhu, Pu Sun, Paolo Sossi and Renqiang Liao for their help and discussions during the preparation of this manuscript. This research was supported by the Key R&D Program of China (2019YFA0708400) and the National Natural Science Foundation of China (42121003, 42122024, 41903035 and 42173051), the MOST Special Fund from the State Key Laboratory of Geological Processes and Mineral Resources and the Special Fund of the State Key Laboratory of Ore Deposit Geochemistry (202201). SL acknowledges support from NSF grant EAR-1946346.

Supplementary materials

Supplementary material associated with this article can be found, in the online version, at doi:10.1016/j.epsl.2023.118499.

References

Brown, E.L., Lesher, C.E., 2016. REEBOX PRO: a forward model simulating melting of thermally and lithologically variable upwelling mantle. Geochem. Geophys. Geosyst. 17, 3929–3968.

Canil, D., O'Neill, H.S.C, 1996. Distribution of ferric iron in some upper-mantle assemblages. J. Petrol. 37, 609–635.

Dai, H.-K., Zheng, J.-P., O'Reilly, S.Y., Griffin, W.L., Xiong, Q., Xu, R., Su, Y.-P., Ping, X.-Q., Chen, F.-K., 2019. Langshan basalts record recycled Paleo-Asian oceanic materials beneath the northwest North China Craton. Chem. Geol. 524, 88–103.

Dauphas, N., Roskosz, M., Alp, E.E., Neuville, D.R., Hu, M.Y., Sio, C.K., Tissot, F.L.H., Zhao, J., Tissandier, L., Médard, E., Cordier, C., 2014. Magma redox and structural controls on iron isotope variations in Earth's mantle and crust. Earth Planet. Sci. Lett. 398, 127–140.

Davis, F.A., Cottrell, E., 2021. Partitioning of Fe_2O_3 in peridotite partial melting experiments over a range of oxygen fugacities elucidates ferric iron systematics in mid-ocean ridge basalts and ferric iron content of the upper mantle. Contrib. Mineral. Petrol. 176, 1–17.

Elkins, L.J., Bourdon, B., Lambart, S., 2019. Testing pyroxenite versus peridotite sources for marine basalts using U-series isotopes. Lithos 332-333, 226–244.

Foden, J., Sossi, P.A., Nebel, O., 2018. Controls on the iron isotopic composition of global arc magmas. Earth Planet. Sci. Lett. 494, 190–201.

Gerbode, C., Dasgupta, R., 2010. Carbonate-fluxed melting of MORB-like pyroxenite at 2.9 GPa and genesis of HIMU ocean island basalts. J. Petrol. 51, 2067–2088.

Ghiorso, M.S., Hirschmann, M.M., Reiners, P.W., Kress III, V.C., 2002. The pMELTS: a revision of MELTS for improved calculation of phase relations and major element partitioning related to partial melting of the mantle to 3 GPa. Geochem. Geophys. Geosyst. 3, 1–35.

Gleeson, M.L.M., Gibson, S.A., 2019. Crustal controls on apparent mantle pyroxenite signals in ocean-island basalts. Geology 47, 321–324.

Gleeson, M.L.M., Gibson, S.A., Williams, H.M., 2020. Novel insights from Fe-isotopes into the lithological heterogeneity of Ocean Island Basalts and plume-influenced MORBs. Earth Planet Sci. Lett. 535, 116114.

Guo, P., Niu, Y., Chen, S., Duan, M., Sun, P., Chen, Y., Gong, H., Wang, X., 2023a. Low-degree melt metasomatic origin of heavy Fe isotope enrichment in the MORB mantle. Earth Planet Sci. Lett. 601.

Guo, P., Niu, Y., Sun, P., Chen, S., Chen, Y., Duan, M., Wang, X., Gong, H., 2023b. Low-Degree Melt Metasomatic Origin of Global Upper Mantle Fe Isotope Fractionation. Geophys. Res. Lett. 50.

He, Y., Meng, X., Ke, S., Wu, H., Zhu, C., Teng, F.-Z., Hoefs, J., Huang, J., Yang, W., Xu, L., Hou, Z., Ren, Z.-Y., Li, S., 2019. A nephelinitic component with unusual δ56Fe in Cenozoic basalts from eastern China and its implications for deep oxygen cycle. Earth Planet Sci. Lett. 512, 175–183.

Herzberg, C., 2011. Identification of source lithology in the hawaiian and canary islands: implications for origins. J. Petrol. 52, 113–146.

Hirschmann, M.M., Kogiso, T., Baker, M.B., Stolper, E.M., 2003. Alkalic magmas generated by partial melting of garnet pyroxenite. Geology 31, 481–484.

Ho, K.-S., Chen, J.-C., Lo, C.-H., Zhao, H.-L., 2003. ^{40}Ar–^{39}Ar dating and geochemical characteristics of late Cenozoic basaltic rocks from the Zhejiang–Fujian region, SE China: eruption ages, magma evolution and petrogenesis. Chem. Geol. 197, 287–318.

Hoernle, K., Tilton, G., Le Bas, M.J., Duggen, S., Garbe-Schönberg, D, 2002. Geochemistry of oceanic carbonatites compared with continental carbonatites: mantle recycling of oceanic crustal carbonate. Contrib. Mineral Petrol. 142, 520–542.

Hoernle, K., White, J.D.L., van den Bogaard, P., Hauff, F., Coombs, D.S., Werner, R., Timm, C., Garbe-Schönberg, D., Reay, A., Cooper, A.F., 2006. Cenozoic intraplate volcanism on New Zealand: upwelling induced by lithospheric removal. Earth Planet Sci. Lett. 248, 350–367.

Hofmann, A.W., 1997. Mantle geochemistry: the message from oceanic volcanism. Nature 385, 219–229.

Johnson, C.M., Bell, K., Beard, B.L., Shultis, A.I., 2009. Iron isotope compositions of carbonatites record melt generation, crystallization, and late-stage volatile-transport processes. Mineral. Petrol. 98, 91–110.

Konter, J.G., Pietruszka, A.J., Hanan, B.B., Finlayson, V.A., Craddock, P.R., Jackson, M. G., Dauphas, N., 2016. Unusual δ^{56}Fe values in Samoan rejuvenated lavas generated in the mantle. Earth Planet Sci. Lett. 450, 221–232.

Lambart, S., Baker, M.B., Stolper, E.M., 2016. The role of pyroxenite in basalt genesis: melt-PX, a melting parameterization for mantle pyroxenites between 0.9 and 5 GPa. J. Geophys. Res. Solid Earth 121, 5708–5735.

Lambart, S., Laporte, D., Schiano, P., 2013. Markers of the pyroxenite contribution in the major-element compositions of oceanic basalts: review of the experimental constraints. Lithos 160-161, 14–36.

Lang, O.I., Lambart, S., 2022. First-row transition elements in pyroxenites and peridotites: a promising tool for constraining mantle source mineralogy. Chem. Geol. 612, 121137.

Le Roux, V., Dasgupta, R., Lee, C.-T.A., 2015. Recommended mineral-melt partition coefficients for FRTEs (Cu), Ga, and Ge during mantle melting. Am. Mineral 100, 2533–2544.

Le Roux, V., Dasgupta, R., Lee, C.T., 2011. Mineralogical heterogeneities in the Earth's mantle: constraints from Mn, Co, Ni and Zn partitioning during partial melting. Earth Planet Sci. Lett. 307, 395–408.

Lei, Y., Li, M., Wang, Z., Zhu, Y., Hu, Z., Liu, Y., Chai, X., 2022. Iron isotopic measurement using large-geometry high-resolution multi-collector inductively coupled plasma mass spectrometer. At Spectrosc. 43, 214–222.

Li, H.-Y., Xu, Y.-G., Ryan, J.G., Huang, X.-L., Ren, Z.-Y., Guo, H., Ning, Z.-G., 2016. Olivine and melt inclusion chemical constraints on the source of intracontinental basalts from the eastern North China Craton: discrimination of contributions from the subducted Pacific slab. Geochim. Cosmochim. Acta 178, 1–19.

Liao, R., Liu, H., Zhu, H., Deng, J., Li, C., Sun, W., 2021. MORB-like δ^{56}Fe values unveil the effect of subduction on the South China Sea basalts. Chem. Geol. 569, 120124.

Liu, S.-A., Wang, Z.-Z., Li, S.-G., Huang, J., Yang, W., 2016. Zinc isotope evidence for a large-scale carbonated mantle beneath eastern China. Earth Planet. Sci. Lett. 444, 169–178.

Macris, C.A., Manning, C.E., Young, E.D., 2015. Crystal chemical constraints on inter-mineral Fe isotope fractionation and implications for Fe isotope disequilibrium in San Carlos mantle xenoliths. Geochim. Cosmochim. Acta 154, 168–185.

Mallik, A., Lambart, S., Chin, E.J., 2021. Tracking the evolution of magmas from heterogeneous mantle sources to eruption. Mantle Convect. Surface Expressions 151–177.

Mallmann, G., O'Neill, H.S.C, 2009. The Crystal/Melt Partitioning of V during Mantle Melting as a Function of Oxygen Fugacity Compared with some other Elements (Al, P, Ca, *Sc*, Ti, Cr, Fe, Ga, Y, Zr and Nb). J. Petrol. 50, 1765–1794.

Matzen, A.K., Wood, B.J., Baker, M.B., Stolper, E.M., 2017. The roles of pyroxenite and peridotite in the mantle sources of oceanic basalts. Nat. Geosci. 10, 530–535.

McGee, L.E., Millet, M.A., Beier, C., Smith, I.E.M., Lindsay, J.M., 2015. Mantle heterogeneity controls on small-volume basaltic volcanism. Geology 43, 551–554.

McGuire, A.V., Dyar, M.D., Nielson, J.E., 1991. Metasomatic oxidation of upper mantle periodotite. Contrib. Mineral. Petrol. 109, 252–264.

Nebel, O., Arculus, R.J., Sossi, P.A., Jenner, F.E., Whan, T.H., 2013. Iron isotopic evidence for convective resurfacing of recycled arc-front mantle beneath back-arc basins. Geophys. Res. Lett. 40, 5849–5853.

Nebel, O., Sossi, P.A., Bénard, A., Arculus, R.J., Yaxley, G.M., Woodhead, J.D., Rhodri Davies, D., Ruttor, S, 2019. Reconciling petrological and isotopic mixing mechanisms in the Pitcairn mantle plume using stable Fe isotopes. Earth Planet. Sci. Lett. 521, 60–67.

Pilet, S., 2015. Generation of low-silica alkaline lavas: petrological constraints, models, and thermal implications. Geological Soc. America Special Papers 514. SPE514-517.

Poitrasson, F., Delpech, G., Grégoire, M., 2013. On the iron isotope heterogeneity of lithospheric mantle xenoliths: implications for mantle metasomatism, the origin of basalts and the iron isotope composition of the Earth. Contrib. Mineral. Petrol. 165, 1243–1258.

Sakuyama, T., Tian, W., Kimura, J.-I., Fukao, Y., Hirahara, Y., Takahashi, T., Senda, R., Chang, Q., Miyazaki, T., Obayashi, M., Kawabata, H., Tatsumi, Y., 2013. Melting of dehydrated oceanic crust from the stagnant slab and of the hydrated mantle transition zone: constraints from Cenozoic alkaline basalts in eastern China. Chem. Geol. 359, 32–48.

Shi, J.-H., Zeng, G., Chen, L.-H., Hanyu, T., Wang, X.-J., Zhong, Y., Xie, L.-W., Xie, W.-L., 2022. An eclogitic component in the Pitcairn mantle plume: evidence from olivine compositions and Fe isotopes of basalts. Geochim. Cosmochim. Acta 318, 415–427.

Shi, J.H., Zeng, G., Chen, L.H., Wang, X.J., Liu, J.Q., Xie, L.W., Yang, Y.H., Zhang, H.L., 2023. Lithology of EM1 Reservoir Revealed by Fe Isotopes of Continental Potassic Basalts. J. Geophys. Res. Solid Earth 128, e2022JB025133.

Sobolev, A.V., Hofmann, A.W., Sobolev, S.V., Nikogosian, I.K., 2005. An olivine-free mantle source of Hawaiian shield basalts. Nature 434, 590–597.

Soderman, C.R., Matthews, S., Shorttle, O., Jackson, M.G., Ruttor, S., Nebel, O., Turner, S., Beier, C., Millet, M.-A., Widom, E., Humayun, M., Williams, H.M., 2021. Heavy δ^{57}Fe in ocean island basalts: a non-unique signature of processes and source lithologies in the mantle. Geochim. Cosmochim. Acta 292, 309–332.

Soderman, C.R., Shorttle, O., Matthews, S., Williams, H.M., 2022. Global trends in novel stable isotopes in basalts: theory and observations. Geochim. Cosmochim. Acta 318, 388–414.

Sossi, P.A., Nebel, O., Foden, J., 2016. Iron isotope systematics in planetary reservoirs. Earth Planet. Sci. Lett. 452, 295–308.

Sossi, P.A., O'Neill, H.S, 2017. The effect of bonding environment on iron isotope fractionation between minerals at high temperature. Geochim. Cosmochim. Acta 196, 121–143.

Sun, P., Niu, Y., Guo, P., Duan, M., Chen, S., Gong, H., Wang, X., Xiao, Y., 2020. Large iron isotope variation in the eastern Pacific mantle as a consequence of ancient low-degree melt metasomatism. Geochim. Cosmochim. Acta 286, 269–288.

Teng, F.-Z., Dauphas, N., Helz, R.T., 2008. Iron Isotope Fractionation During Magmatic Differentiation in Kilauea Iki Lava Lake. Science 320, 1620–1622.

Teng, F.-Z., Dauphas, N., Huang, S., Marty, B., 2013. Iron isotopic systematics of oceanic basalts. Geochim. Cosmochim. Acta 107, 12–26.

Timm, C., Hoernle, K., Van Den Bogaard, P., Bindeman, I., Weaver, S, 2009. Geochemical Evolution of Intraplate Volcanism at Banks Peninsula, New Zealand: interaction Between Asthenospheric and Lithospheric Melts. J. Petrol. 50, 989–1023.

Wang, X.J., Chen, L.H., Hanyu, T., Shi, J.H., Zhong, Y., Kawabata, H., Miyazaki, T., Hirahara, Y., Takahashi, T., Senda, R., Chang, Q., Vaglarov, B.S., Kimura, J.I., 2021. Linking Chemical Heterogeneity to Lithological Heterogeneity of the Samoan Mantle Plume With Fe-Sr-Nd-Pb Isotopes. J. Geophys. Res. Solid Earth 126, e2021JB022887.

Weyer, S., Ionov, D.A., 2007. Partial melting and melt percolation in the mantle: the message from Fe isotopes. Earth Planet. Sci. Lett. 259, 119–133.

White, W.M., 2010. Oceanic Island Basalts and Mantle Plumes: the Geochemical Perspective. Annu. Rev. Earth Planet. Sci. 38, 133–160.

Williams, H.M., Bizimis, M., 2014. Iron isotope tracing of mantle heterogeneity within the source regions of oceanic basalts. Earth Planet. Sci. Lett. 404, 396–407.

Workman, R.K., Hart, S.R., 2005. Major and trace element composition of the depleted MORB mantle (DMM). Earth Planet. Sci. Lett. 231, 53–72.

Xu, R., Liu, Y., Lambart, S., 2020a. Melting of a hydrous peridotite mantle source under the Emeishan large igneous province. Earth Sci. Rev. 207, 103253.

Xu, R., Liu, Y., Lambart, S., Hoernle, K., Zhu, Y., Zou, Z., Zhang, J., Wang, Z., Li, M., Moynier, F., Zong, K., Chen, H., Hu, Z., 2022. Decoupled Zn-Sr-Nd isotopic composition of continental intraplate basalts caused by two-stage melting process. Geochim. Cosmochim. Acta 326, 234–252.

Xu, R., Liu, Y., Wang, X., Zong, K., Hu, Z., Chen, H., Zhou, L., 2017. Crust recycling induced compositional-temporal-spatial variations of Cenozoic basalts in the Trans-North China Orogen. Lithos 274, 383–396.

Xu, R., Liu, Y., Wang, X.-C., Foley, S.F., Zhang, Y., Yuan, H., 2020b. Generation of continental intraplate alkali basalts and implications for deep carbon cycle. Earth Sci. Rev. 201, 103073.

Xu, Y., Li, H., Hong, L., Ma, L., Ma, Q., Sun, M., 2018. Generation of Cenozoic intraplate basalts in the big mantle wedge under eastern Asia. Sci. China Earth Sci. 61, 869–886.

Yang, Z.-F., Li, J., Liang, W.-F., Luo, Z.-H., 2016. On the chemical markers of pyroxenite contributions in continental basalts in Eastern China: implications for source lithology and the origin of basalts. Earth Sci. Rev. 157, 18–31.

Yang, Z.-F., Zhou, J.-H., 2013. Can we identify source lithology of basalt? Sci. Rep. 3, 1856.

Yang, Z.F., Li, J., Jiang, Q.B., Xu, F., Guo, S.Y., Li, Y., Zhang, J., 2019. Using major element logratios to recognize compositional patterns of basalt: implications for source lithological and compositional heterogeneities. J. Geophys. Res. Solid Earth 124, 3458–3490.

Zeng, G., Chen, L.-H., Xu, X.-S., Jiang, S.-Y., Hofmann, A.W., 2010. Carbonated mantle sources for Cenozoic intra-plate alkaline basalts in Shandong, North China. Chem. Geol. 273, 35–45.

Zou, Z., Wang, Z., Foley, S., Xu, R., Geng, X., Liu, Y.-N., Liu, Y., Hu, Z., 2022. Origin of low-MgO primitive intraplate alkaline basalts from partial melting of carbonate-bearing eclogite sources. Geochim. Cosmochim. Acta 324, 240–261.